Flight Dynamics of Boomerangs: Impact of Joint Angle

Ethan Foss,[1]
University of California at San Diego, La Jolla, California 92093, USA

Jaime Alvarez,[2]
Qualcomm Technologies Incorporated, San Diego, California 92121, USA

Todd Hunt,[3]
Stanford University, Stanford, California 94305, USA

and
Prasad Gudem,[4]
University of California at San Diego, La Jolla, California 92093, USA

Prior work on the study of flight trajectory of boomerangs focused on tri-bladder design instead of the traditional–V boomerangs due to simplicity of analysis. In this paper, we study the impact of joint angle of traditional–V boomerangs on their flight trajectories. An ultra-compact, custom UWB wireless positioning tag that is small enough to embed in the arms of a traditional–V boomerang without impacting the aerodynamics of the boomerang was developed. Flight trajectories of 3D printed traditional–V boomerangs with joint angles of 30^0, 50^0, 70^0, 90^0, 110^0 and 130^0 were measured using meshed UWB wireless positioning system. The measured flight trajectories for different joint angles were compared with the simulation results.

[1] Undergraduate student, Department of Mechanical and Aerospace Engineering
[2] ATE Engineer, Product and Test Group
[3] Graduate student, Department of Aeronautics and Astronautics
[4] Adjunct Professor, Department of Electrical and Computer Engineering

Nomenclature

m = Boomerang mass (kg)

I_x, I_y, I_z = Boomerang moments of inertia (kgm^2)

X = X-Position of Boomerang (m)

X = X-Position of Boomerang (m)

Y = Y-Position of Boomerang (m)

Z = Z-Position of Boomerang (m)

V_x = X-Velocity of Boomerang (m/s)

V_y = Y-Velocity of Boomerang (m/s)

V_z = Z-Velocity of Boomerang (m/s)

ϕ, θ, ξ = Euler Angles of Boomerang (rad)

ω_1 = Rotational Velocity about Body-1 Axis of Boomerang (rad/s)

ω_2 = Rotational Velocity about Body-2 Axis of Boomerang (rad/s)

ω_3 = Rotational Velocity about Body-3 Axis of Boomerang (rad/s)

T_{ib} = Coordinate Transformation Matrix from Body-Frame to Inertial-Frame

F_x, F_y, F_z = Inertial frame forces acting on Boomerang (N)

M_1, M_2, M_3 = Body frame moments acting on Boomerang (Nm)

$\boldsymbol{V_{f,i}}$ = Body-frame velocity vector parallel to ith airfoil segment (m/s)

$\boldsymbol{\omega}$ = Body-frame rotational velocity vector (rad/s)

$\boldsymbol{V_B}$ = Body-frame Boomerang velocity vector (m/s)

$\boldsymbol{r_i}$ = Body-frame position vector from centroid to airfoil segment center of pressure (m)

$\boldsymbol{f_1}$ = Airfoil direction of first blade

$\boldsymbol{f_2}$ = Airfoil direction of second blade

$\hat{\boldsymbol{z}}$ = Unit Length Z-axis ($[0 \quad 0 \quad 1]^T$)

$V_{F,i}$ = Velocity Magnitude at ith airfoil segment (m/s)

ρ = Ambient air density (kg/m^3)

C_{L0+} = Leading Edge Basic Lift Coefficient

$C_{L\alpha+}$ = Leading Edge AOA Lift Coefficient (rad^{-1})

C_{D0+} = Leading Edge Basic Drag Coefficient

$C_{D\alpha+}$ = Leading Edge AOA Lift Coefficient (rad^{-1})

C_{L0-} = Trailing Edge Basic Lift Coefficient

$C_{L\alpha-}$ = Trailing Edge AOA Lift Coefficient (rad^{-1})

C_{D0-} = Trailing Edge Basic Drag Coefficient

$C_{D\alpha-}$ = Trailing Edge AOA Lift Coefficient (rad^{-1})

α_B = Boomerang Angle of Attack (rad)

D_i = Drag Magnitude at ith airfoil segment (N)

L_i = Lift Magnitude at ith airfoil segment (N)

$\boldsymbol{D_i}$ = Drag Vector at ith airfoil segment (N)

$\boldsymbol{L_i}$ = Lift Vector at ith airfoil segment (N)

N = Finite Element Segment Count

$\boldsymbol{F_B}$ = Body-Frame Boomerang Forces

$\boldsymbol{M_B}$ = Body-Frame Boomerang Moments

$\boldsymbol{F}$ = Inertial-Frame Boomerang Forces

I. Introduction

Boomerangs are one of the oldest flying manmade objects that still intrigue scientists worldwide. Originating from Australia a few thousand years ago, the returning boomerang was discovered only recently by outsiders. It is believed that returning boomerangs were originally used for entertainment, but there is some evidence that they might have also been used to hunt flocks of birds. Nowadays, boomerangs come in a nearly infinite number of shapes and sizes, each with unique flight properties. Some of these are used for the sport of competitive boomerang throwing and catching, where impressive feats of athleticism are achieved. A few types of popular competition boomerangs are depicted in **Figure 1** [1]. Over the last two decades, boomerang throwers have developed empirical methods to predict the flight trajectories of boomerangs of different shapes. However, theoretical understanding of how the flight trajectory of boomerangs is impacted by the shape is incomplete at best.

In the 1970's, Felix Hess [2] conducted a theoretical study of the flight dynamics of boomerangs by deriving the necessary equations for numerical simulation of the flight trajectories. He also developed a simplified model for a circular flight path of a boomerang, often referred to as Hess's model. In 2004, in a two-part study, Azuma Beppu et. al. [3, 4] simulated the flight trajectory of boomerangs with various initial launch conditions and joint angle of the boomerang. In 2012, John Vassberg [5] used blade element theory to derive expressions for lift and rolling moment and showed that Hess's model over predicts lift and rolling moment. Using the simplified equations derived from blade element theory an expression for the radius of the circular flight trajectory was derived. This will be referred to as Vassberg's model. Recently, Gudem et. al. [6, 7] extended Vassberg's analysis of blade element theory by including the effect of reversal of airflow over the trailing edge and compared the simulation results of lift with experimental measurements from the wind tunnel. Despite significant progress on the aerodynamics of boomerang on the theoretical side, until recent no reliable measurement data of the flight trajectory of boomerangs was available. In 2020, Gudem et. al. [8] measured the flight trajectory of a tri-bladder boomerangs using ultra-wide band (UWB) wireless positioning and compared with the simulation results. The commercial electronic UWB wireless positioning tag was placed at the center of the tri-bladder to minimize the impact on the aerodynamics of the boomerang. The commercial UWB system used in the study is capable of measurements within 10-centimeter accuracy, far superior to 10-meter accuracy achievable using global position system (GPS).

Prior work [2, 5] on the study of flight trajectory focused on tri-bladder boomerangs instead of the traditional–V boomerangs due to simplicity of design and analysis. In this paper, we study the impact of joint angle on the flight

trajectory of traditional–V boomerangs. A custom UWB wireless positioning tag that is ultra-compact and capable of embedding in the arms of a traditional–V boomerang without impacting the aerodynamics of the boomerang was developed. 3D printed traditional–V boomerangs with joint angles of 30^0, 50^0, 70^0, 90^0, 110^0 and 130^0 were used in the study.

This paper is organized as follows. In section II, we describe the design of the 3D printed boomerangs with various joint angles used in this study. In section III, we describe the ultra-compact custom UWB wireless positioning tag developed for this project. A meshed ultra-wideband wireless positioning system described in prior publication was used to accurately track the flight trajectory of the boomerangs. A brief overview of this wireless positioning system is provided for the sake of completeness. In section IV, we summarize the equations of motion and analytical expressions used in the simulation of flight trajectory of traditional–V boomerang. In section V, we compare the simulation results of the flight trajectory of boomerangs with different joint angles with experimental measurements from UWB wireless positioning system. Section VI provides the conclusions.

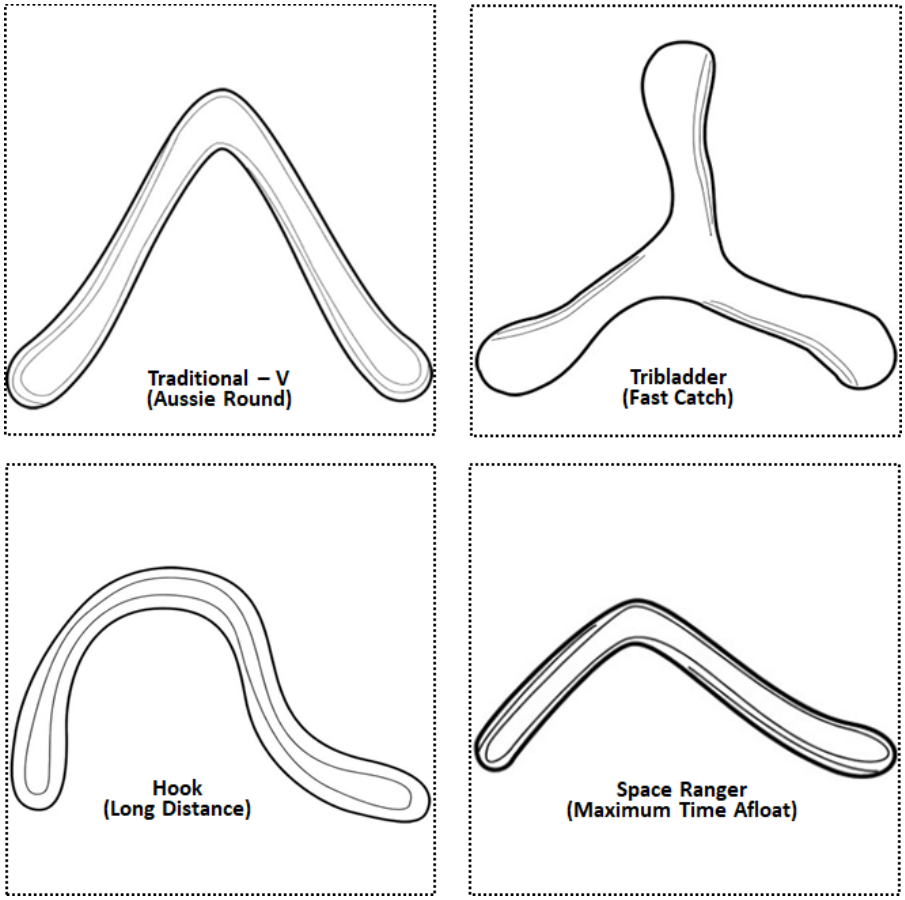

Fig. 1: Sample of boomerangs used in competitive championships [1].

II. 3D Printed Boomerangs with Varying Joint Angles

SolidWorks was used to create the design of the traditional–V boomerangs as shown in **Figure 2**. The airfoil used was the Rhode Saint Genessee 32. The sketch of this airfoil was extruded, and then circular patterned about the origin. The two blades were then merged and fileted. Components were also cut out to make room for the UWB chip, LiPo battery, and wiring. The boomerang was constructed such that the blade length is measured from the origin of the boomerang ensuring boomerang volume is invariant across all joint angles. The physical parameters of the traditional–V boomerangs is shown in **Table I**.

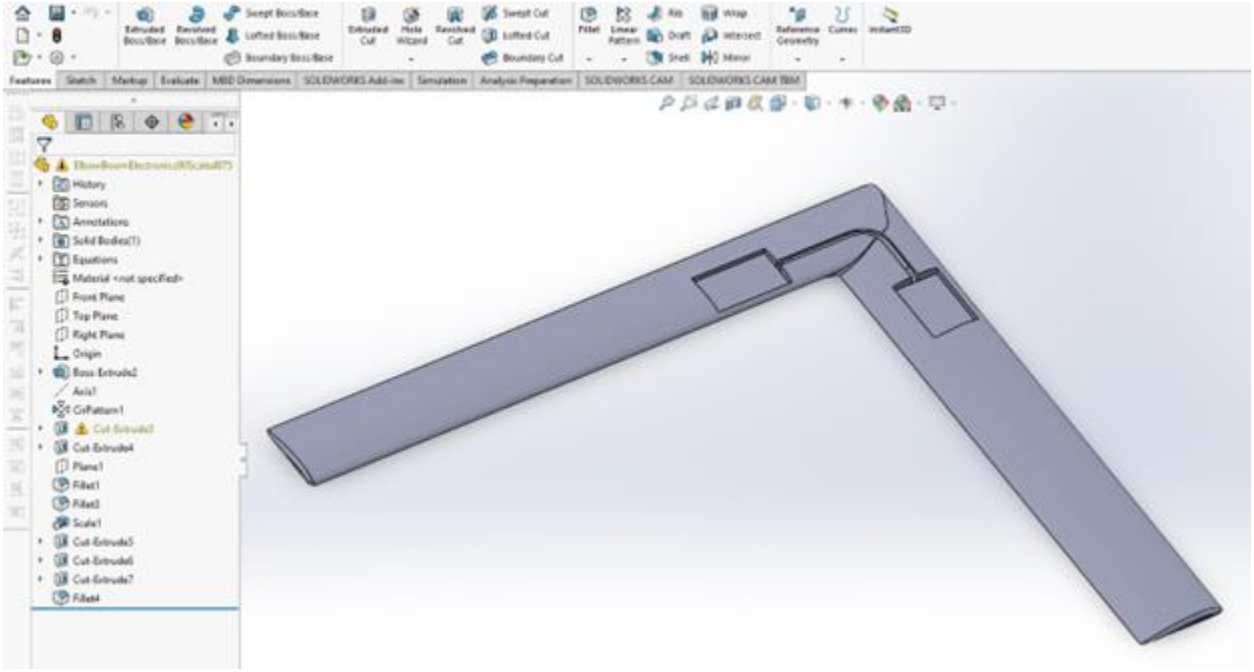

Fig. 2: Traditional–V Boomerang Design in SolidWorks

Table I: Traditional – V Boomerang Physical Parameters

Traditional–V Boomerang Physical Parameters	
Blade Length	27cm
Chord Length	3.87cm
Blade Thickness	0.468cm
Blade Pitch	0deg
Final Mass	50g

Ultimaker Cura Slicer was used to convert the Boomerang Geometry into Geometric Code for the 3D printer to read and print. Slicer settings shown in **Table II** were used for the boomerang. These settings produce a traditional–V boomerangs that weighs approximately 50 grams.

Table II: Traditional – V Boomerang Printer Settings

Traditional–V Boomerang Printer Settings	
Layer Height	0.16mm
Wall Line Count	3
Top/Bottom Layer Count	4
Infill	45%

A Creality3D CR10S5 3D printer shown in **Figure 3** was used to print the traditional–V boomerangs. A TH3D Ezabl Auto Bed Leveler was used to ensure consistency in prints. This printer has a 0.4mm extruder nozzle, and eSun PLA+ filament was used. The extruder printing temperature was 215C, and the bed temperature was 62C.

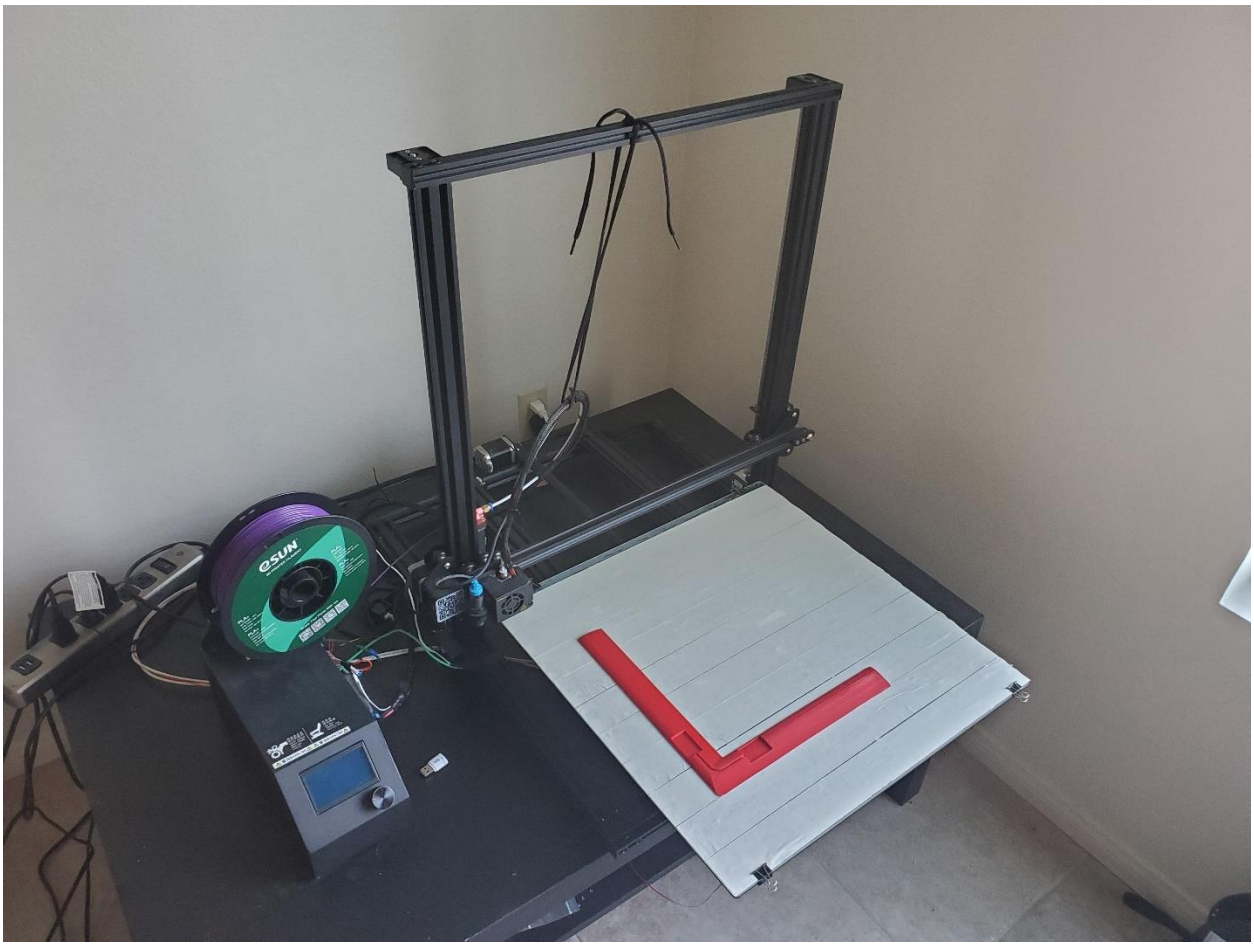

Fig. 3: Creality3D CR10S5 3D Printer used to Print Traditional–V Boomerangs

3D printed traditional–V boomerangs with joint angles of 30^0, 50^0, 70^0, 90^0, 110^0 and 130^0 used in the study are shown in **Figure 4**.

Fig. 4: Traditional–V 3D Printed Boomerangs with Varying Joint Angles

III. Ultra-Compact Custom UWB Wireless Tag and Positioning System

Ultra-Compact Custom UWB Wireless Tag

An ultra-compact, custom UWB wireless positioning tag shown in **Figure 5** was developed using Qorvo/Decawave DWM1001C chip. It is small enough to embed in the arms of a traditional–V boomerang without impacting the aerodynamics of the boomerang. The ultra-compact custom UWB wireless tag and LiPo battery were embedded in the boomerang. The ultra-compact custom UWB wireless tag and LiPo battery and the battery weigh less than 5g and approximately match the weight of the 3D printed plastic removed to embed the components. The

compartment built for the electronics was sealed with a plastic tape to minimize the impact on the aerodynamics of the boomerangs.

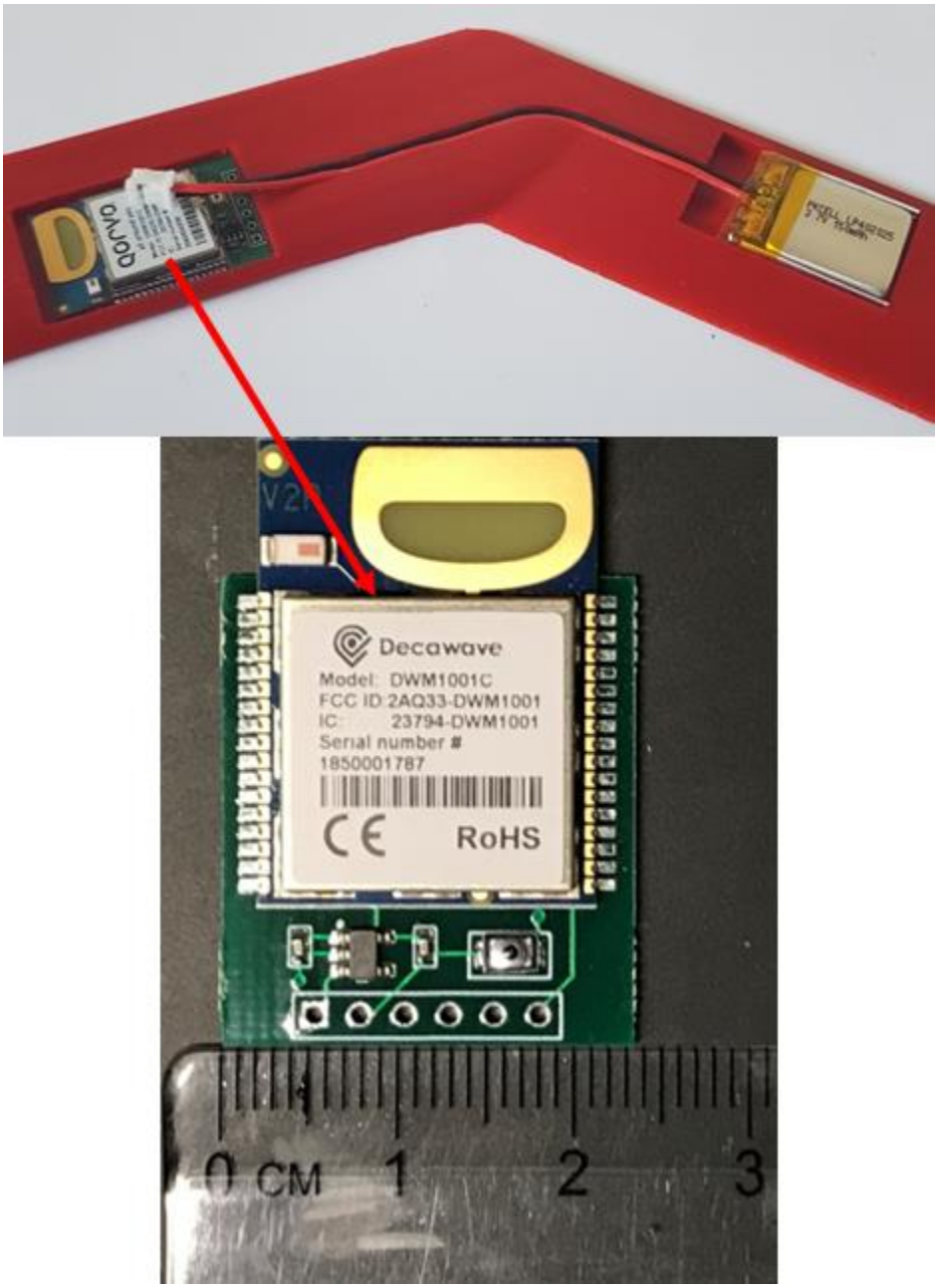

Fig. 5: Ultra-Compact Custom UWB Wireless Positioning Tag

The key component of the ultra-compact, custom UWB wireless positioning tag is an 802.15.4 compliant [14] DW1000 UWB transceiver [15]. A simplified block diagram of the DW1000 transceiver is shown in **Figure 6**. The RF receiver frontend consists of a low-noise amplifier (LNA) followed by a down-converter (DnC). The RF receiver frontend is followed by the analog baseband filter and analog-to-digital (ADC) converter. The ADC output is

processed by the digital RX module. On the transmitter side, the output of the digital TX module drives the pulse generator followed by the up-converter (UpC) and a driver amplifier (DA). The transceiver supports UWB channels 1 to 7 and can be configured in 500MHz or 900MHz bandwidth modes. Channel 5 (6240-6739MHz) was selected to keep the antenna size compact.

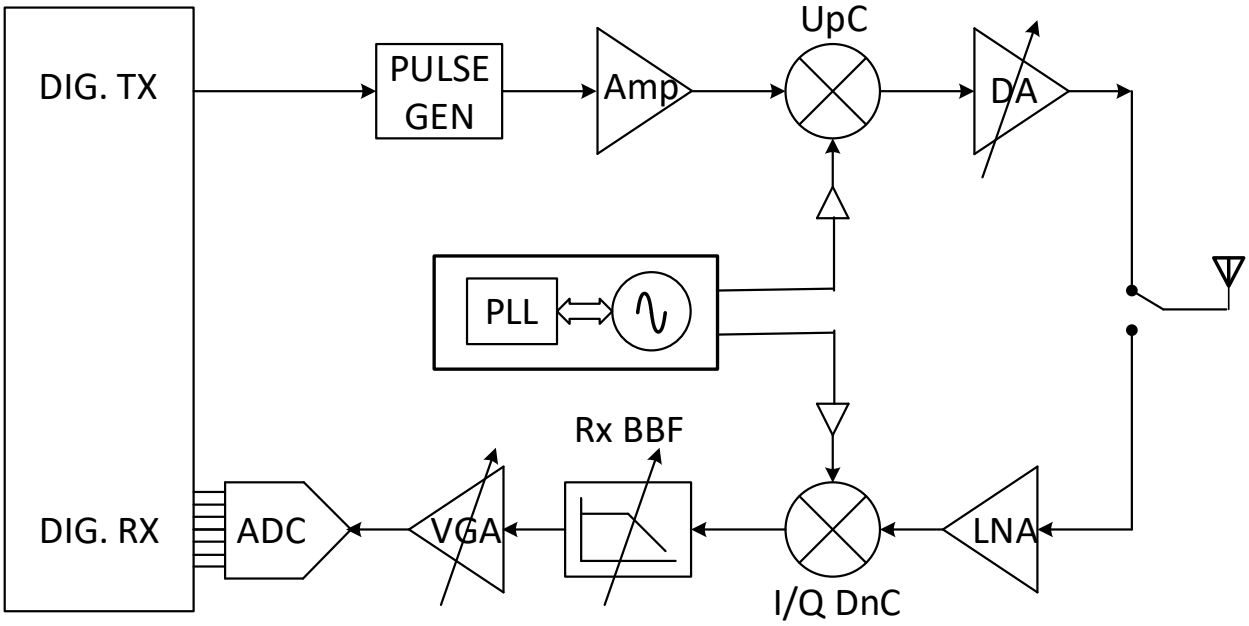

Fig. 6: DWM1001 UWB Wireless Transceiver

UWB Wireless Positioning System

UWB wireless technology utilizes 3.1 – 10.6GHz unlicensed spectrum for short-range high-speed data communication and position location. UWB has a signal bandwidth of over 500MHz or at least 20% of its center frequency. An emission limit of –41.3dBm/MHz (75nW/MHz) was imposed to avoid interference with deployment of licensed radios [12]. Unlike GPS which is limited to 10m level accuracy under "static" conditions, UWB is capable of achieving accuracy levels below 10-centimeters under "dynamic" conditions. The superior accuracy of the UWB system along with better penetration through materials such as wood and plastic make it the ideal choice for tracking boomerangs. Although UWB offers superior accuracy compared to GPS, its range is limited to only 10-meters. To extend the range, a meshed network of 16 anchors was deployed to track the boomerang flight. Further details of the UWB wireless positioning system are described in [].

IV. Equations for Simulation of Traditional–V Boomerangs

A 6 degree-of-freedom trajectory simulation was developed in MATLAB to study the dynamics and aerodynamics of the traditional–V boomerang at different joint angles. As illustrated in **Figure 6**, traditional–V boomerang was treated as a point mass at its center of mass, which is a function of the joint angle, γ, as well as the chord length, C, and blade length, L.

$$D = \frac{\frac{3}{2}C^2 - 6L^2 - \frac{C^2}{2}\cos(\gamma) + 6L^2\cos(\gamma)}{12L(\cos(\gamma) - 1)}\cos\left(\frac{\gamma}{2}\right) \tag{1}$$

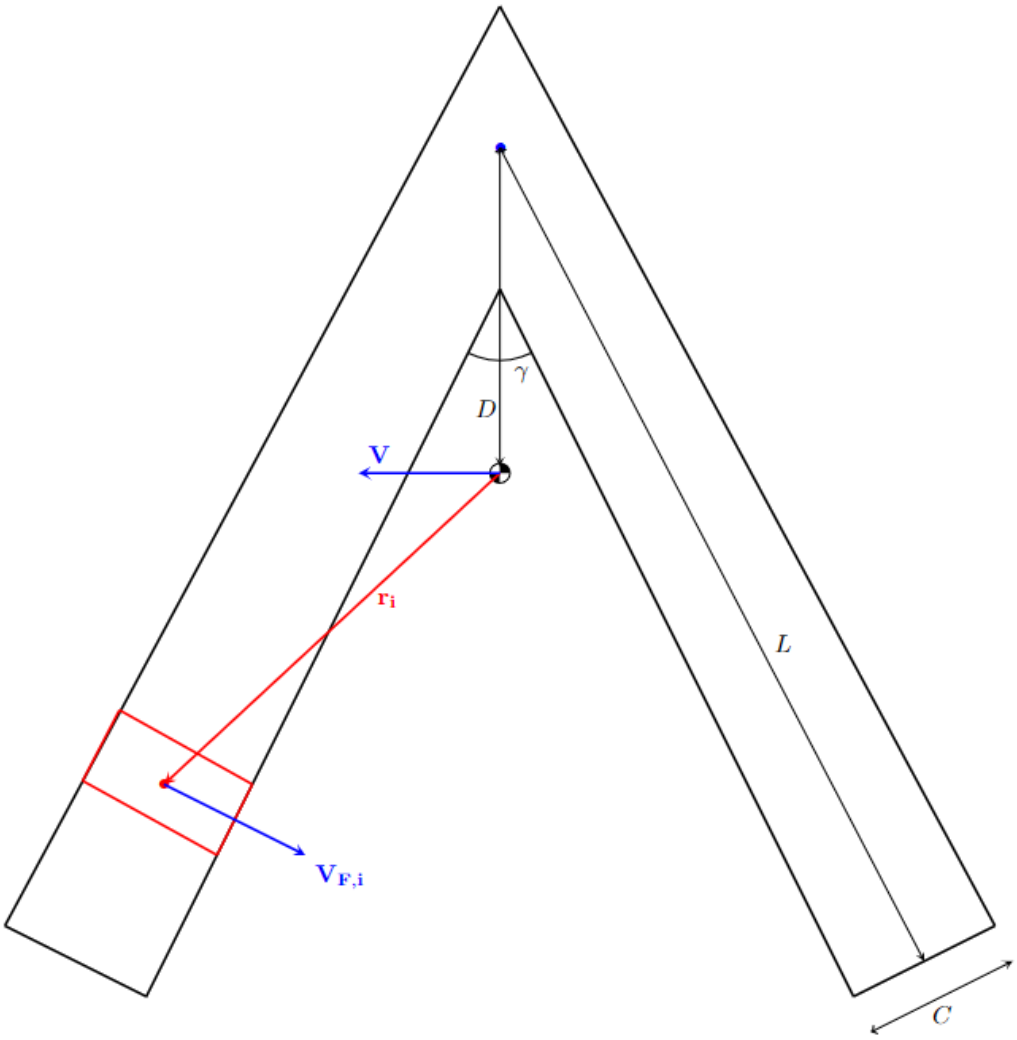

Fig. 7: Illustration of the Traditional–V Boomerang

The moments of inertia for the boomerang about its center of mass are determined by calculating the moments of inertia of the two boomerang blades about the boomerang origin, and then translating back to the center of mass.

$$I_x = m\frac{C^2 - C^2\sin\left(\frac{\gamma}{2}\right) + 4L^2\sin^2\left(\frac{\gamma}{2}\right) + T^2}{12} \tag{2}$$

$$I_y = m\frac{C^4\sin^4\left(\frac{\gamma}{2}\right) - C^4\sin^2\left(\frac{\gamma}{2}\right) + C^4\sin^6\left(\frac{\gamma}{2}\right) - C^4 + 48L^4\sin^4\left(\frac{\gamma}{2}\right) - 48L^4\sin^6\left(\frac{\gamma}{2}\right) + 24C^2L^2\sin^2\left(\frac{\gamma}{2}\right) + 24C^2L^2\sin^6\left(\frac{\gamma}{2}\right) + 48L^2T^2\sin^4\left(\frac{\gamma}{2}\right)}{288L^2\sin^4\left(\frac{\gamma}{2}\right)} \tag{3}$$

$$I_z = m\frac{C^4\sin^4\left(\frac{\gamma}{2}\right) - C^4\sin^2\left(\frac{\gamma}{2}\right) + C^4\sin^6\left(\frac{\gamma}{2}\right) - C^4 + 48L^4\sin^4\left(\frac{\gamma}{2}\right) + 144L^4\sin^6\left(\frac{\gamma}{2}\right) + 24C^2L^2\sin^2\left(\frac{\gamma}{2}\right) + 48C^2L^2\sin^4\left(\frac{\gamma}{2}\right) - 24C^2L^2\sin^6\left(\frac{\gamma}{2}\right)}{288L^2\sin^4\left(\frac{\gamma}{2}\right)} \tag{4}$$

With the mass properties of the traditional–V boomerang established; the dynamics can be developed. To transform between the inertial frame, attached to the ground, and the body frame, attached to and spinning with the traditional–V boomerang, the following coordinate transformation matrix is used, which is a function of the Euler angles describing the orientation of the traditional–V boomerang.

$$T_{ib} = \begin{bmatrix} c\phi c\psi + s\phi s\theta s\xi & c\phi s\xi - s\phi s\theta c\xi & -s\phi c\theta \\ s\phi c\xi - c\phi s\theta s\xi & s\phi s\xi + c\phi s\theta c\xi & c\phi c\theta \\ c\theta s\xi & -c\theta c\xi & s\theta \end{bmatrix} \tag{5}$$

A state vector is defined to describe the state of the traditional–V boomerang at a given instant,

$$\boldsymbol{x} = [X \quad Y \quad V_x \quad V_y \quad V_z \quad \phi \quad \theta \quad \xi \quad \omega_1 \quad \omega_2 \quad \omega_3]^T \tag{6}$$

And the equations of motion for this state vector are defined, using Euler's Equations of Translation and Rotation.

$$\dot{\boldsymbol{x}} = \begin{bmatrix} V_x \\ V_y \\ V_z \\ F_x/m \\ F_y/m \\ F_z/m \\ \sin(\xi)\sec(\theta)\,\omega_1 - \cos(\xi)\sec(\theta)\,\omega_2 \\ \cos(\xi)\,\omega_1 + \sin(\xi)\,\omega_2 \\ -\tan(\theta)\sin(\xi)\,\omega_1 + \tan(\theta)\cos(\xi)\,\omega_2 - \omega_3 \\ (M_1 + (I_y - I_z)\omega_2\omega_3)/I_x \\ (M_2 + (I_z - I_x)\omega_1\omega_3)/I_y \\ (M_3 + (I_x - I_y)\omega_1\omega_2)/I_z \end{bmatrix} \tag{7}$$

The forces and moments acting on the traditional–V boomerang can be determined with an extension of blade element theory. Unlike previous papers, these forces and moments are determined numerically, rather than analytically, due to the complex nature of the traditional–V boomerang. The blade is divided into finite element segments, and the forces and moments are numerically integrated. The velocity of the ith finite element along the airfoil direction is defined as follows:

$$\boldsymbol{V_{F,i}} = (\boldsymbol{\omega} \times \boldsymbol{r_i} + \boldsymbol{V_B}) \tag{8}$$

The x and z components of this Velocity vector are extracted with the following:

$$V_{x,i} = \boldsymbol{V_{F,i}} \cdot \boldsymbol{f_1} \tag{9}$$

$$V_{z,i} = \boldsymbol{V_{F,i}} \cdot \hat{\boldsymbol{z}} \tag{10}$$

The velocity magnitude that the airfoil experiences is determined by the norm of these two quantities

$$V_{F,i} = \sqrt{V_{x,i}^2 + V_{z,i}^2} \tag{11}$$

The magnitude of the drag and lift forces on the airfoil segment can be determined from the drag/lift coefficients, $V_{F,i}$, the area of the segment, the boomerang angle of attack, and the ambient air density. The drag/lift coefficients are determined by the direction of the airflow; if the airflow is anti-parallel to the airfoil, then trailing edge coefficients are used, whereas if the flow is parallel to the airfoil, leading edge coefficients are used. A small angle approximation is also used for the airfoils. Rhode Saint Genesee 32 is used in 3D printed boomerangs. Lift and drag coefficients of the Rhode Saint Genesee 32 airfoil are shown in **Table III**.

Table III: Lift and Drag Coefficients of the Airfoil

RSG32 Airfoil Lift and Drag Coefficients for Simulation		
Drag Coefficient	Leading Edge	Trailing Edge
Basic Lift Coefficient (C_{l0})	0.617	-0.617
AOA Lift Coefficient ($C_{l\alpha}$) per radian	5.3	5.3
Basic Drag Coefficient (C_{D0})	0.01526	0.01526
AOA Drag Coefficient ($C_{D\alpha}$) per radian	0.115	0.115

$$C_L = C_{L0+} + C_{L\alpha+}\alpha_B,\ C_D = C_{D0+} + C_{D\alpha+}\alpha_B \text{ if leading edge flow} \tag{12}$$

$$C_L = C_{L0-} + C_{L\alpha-}\alpha_B\ ,\ C_D = C_{D0-} + C_{D\alpha-}\alpha_B \text{ if trailing edge flow} \tag{13}$$

$$\alpha_B = \sin^{-1}\left(\frac{\boldsymbol{V_B} \cdot \hat{\boldsymbol{z}}}{V_B}\right) \tag{14}$$

The Lift and Drag magnitudes and directions at the airfoil segment are given by

$$\boldsymbol{L_i} = L_i\, \hat{\boldsymbol{z}} \tag{15}$$

$$D_i = \frac{1}{2}\rho A_i D V_{F,i}^2 \tag{16}$$

$$\boldsymbol{L_i} = L_i\, \hat{\boldsymbol{z}} \tag{17}$$

$$\boldsymbol{D_i} = -D_i\, \boldsymbol{f_1} \tag{18}$$

Finally, the Lift and Drag forces are summed across the entire blade to determine the resulting forces and moments

$$\boldsymbol{F_B} = \sum_{i=1}^{N} \boldsymbol{L_i} + \sum_{i=1}^{N} \boldsymbol{D_i} \tag{19}$$

$$\boldsymbol{M_B} = \sum_{i=1}^{N} \boldsymbol{r_i} \times \boldsymbol{L_i} + \sum_{i=1}^{N} \boldsymbol{r_i} \times \boldsymbol{D_i} \tag{20}$$

The force vector can be transformed back into the inertial frame, and then summed with the gravity force vector.

$$\boldsymbol{F} = T_{ib}\boldsymbol{F_B} - mg\hat{\boldsymbol{z}} \tag{21}$$

With the forces and moments determined, along with the equations of motion for the traditional–V boomerang state, the trajectory can be determined via an RK4 numerical integration method.

V. Comparison of Simulation Results with Experimental Measurements

Boomerangs with joint angles below 30^0 and above 150^0 were experimentally found to be unstable. Therefore, in this work, our primary focus has been on studying the flight trajectory of boomerangs with joint angles from 50^0 to 130^0. Moments of inertia about the X, Y and Z-axis of the traditional–V boomerangs obtained from equations (2) – (4) is shown in **Figure 8**. As the joint angle is swept from 50^0 to 130^0, the moment of inertia about the X-axis and Z-axis increases approximately linear, while the moment of inertia about the Y-axis decreases approximately linear. Moments of inertia strongly influence the precession and nutation of the boomerang under identical throw conditions.

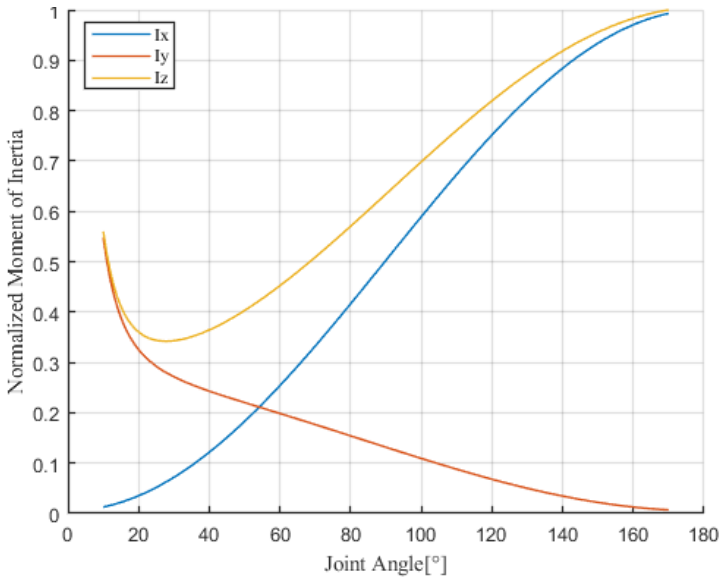

Fig. 8: Moment of Inertia of Traditional–V Rangs vs. Joint Angle

Using the equations (1) – (21) described in section V, the flight trajectory of boomerangs with joint angles of 30^0, 50^0, 70^0, 90^0, 110^0 and 130^0 were simulated. Traditional–V boomerangs with joint angles ranging from 30^0, 50^0, 70^0, 90^0, 110^0 and 130^0 were thrown in an open field in the early morning during very light wind conditions. While UWB wireless positioning system can achieve centimeter level accuracy for X, Y and Z, it cannot measure the measure the Euler angles ψ, ϕ, and θ. A video imaging approach was used to measure the rotation speed using three 4K GoPro cameras. The approximate rotation speed of the boomerang over the duration of the flight was obtained by processing the video frames. Initial throw conditions used in the simulation are shown in **Table IV**.

Table IV: Initial Boomerang Launch Conditions

Simulation Throw Parameters	
Initial Velocity	16m/s
Initial Rotational Rate	9Hz
Throw Height	1.8m
Horizontal Throw Angle	10deg
Layover Throw Angle	15deg
Initial AOA	0deg

Simulation results of the X and Y positions vs. time were compared with measurements obtained from the UWB wireless positioning system. As shown in **Figure 9**, the simulation results and measurements match reasonably well. Simulation and measurement results of the flight trajectory are also shown in **Figure 10**. The measured data exhibits the classic "tear" drop shaped trajectory seen in many boomerang videos. Further research is necessary to close the remaining gaps between simulation and measurement.

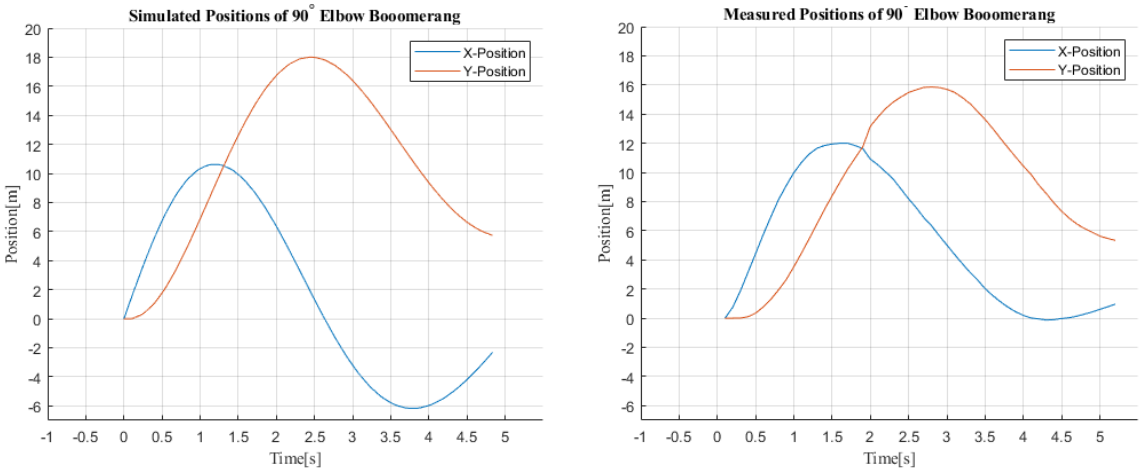

Fig. 9: Simulated and Measured X and Y Positions vs. Time of the 90^0 Traditional–V Rang

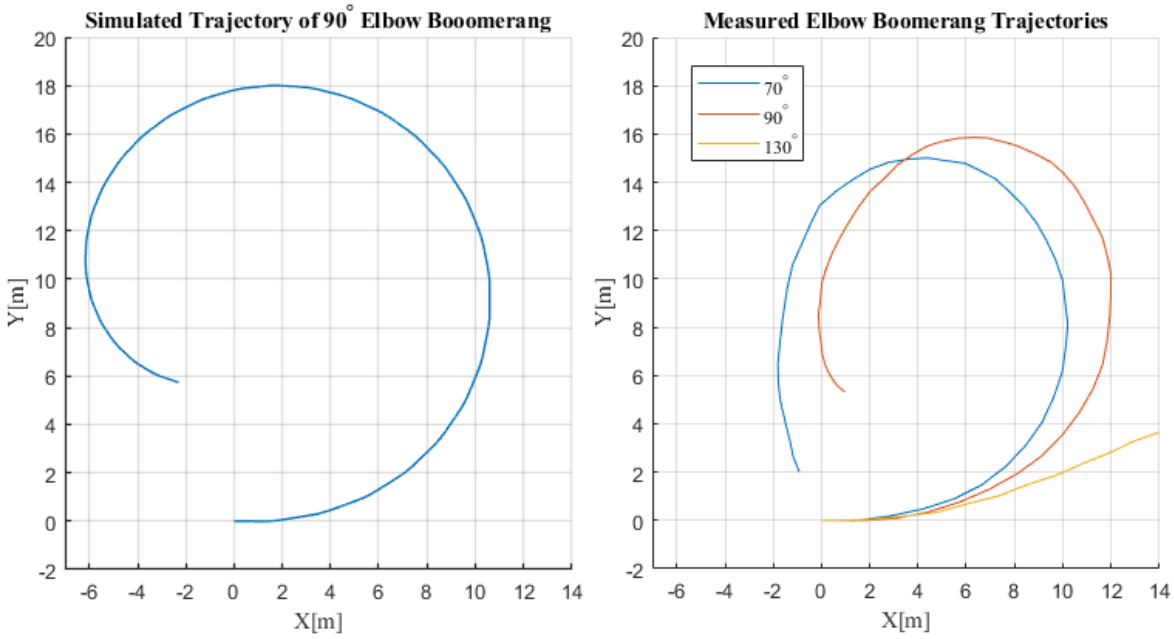

Fig. 10: Simulated and Measured Trajectory (X vs. Y Positions) of the Traditional–V Boomerangs

VI. Conclusion

Prior work on the study of flight trajectory of boomerangs focused on tri-bladder design instead of the traditional–V boomerangs due to simplicity of analysis. In this paper, we studied the impact of joint angle of traditional–V boomerangs on their flight trajectories. A custom UWB wireless positioning tag that is ultra-compact and capable of embedding in the arms of a traditional–V boomerang without impacting the aerodynamics of the boomerang was developed. A meshed ultra-wideband wireless tracking system was used to accurately track the flight trajectory of the boomerang. Flight trajectories of 3D printed traditional–V boomerangs with joint angles of from 30^0, 50^0, 70^0, 90^0, 110^0 and 130^0 were measured using meshed UWB wireless positioning system. The measured flight trajectories for different joint angles were compared with the simulation results. The simulation results show reasonable agreement with measured data. Further research is necessary to close the remaining gaps between simulation and measurement.

References

[1] John Cross, "Performance Boomerangs," 2012. 2nd edition.

[2] F. Hess, "Boomerangs, Aerodynamics and Motion," Ph.D. Thesis, Groningen University, June 1975.

[3] Akira Azuma, Goro Beppu, Hiroaki Ishikawa, and Kunio Yasuda, "Flight Dynamics of the Boomerang, Part 1: Fundamental Analysis," Journal of Guidance, Control, and Dynamics, Vol. 27, No. 4, 2004, pp. 545-554.

[4] Goro Beppu, Hiroaki Ishikawa, Akira Azuma, and Kunio Yasuda, "Flight Dynamics of the Boomerang, Part 2: Effects of Initial Condition and Geometrical Configuration," Journal of Guidance, Control, and Dynamics, Vol. 27, No. 4, 2004, pp. 555-563.

[5] John Vassberg, "Boomerang Flight Dynamics," 30th AIAA Applied Aerodynamics Conference, 2012.

[6] P. Gudem, M. Schütz, K. Holland, "Flight Dynamics of Boomerangs: Impact of reversal of airflow and reversal of angle of attack", AIAA Aviation Forum and Exposition, 2019.

[7] J. Tahmassebpur, M. Laslett, M. Schütz and P. Gudem, "Wind Tunnel Measurements of Non-Dimensional Lift Coefficient of a Boomerang and Comparison to Theory," AIAA Aviation Forum and Exposition, 2021.

[8] P. Gudem, M. Laslett, G. Carfano, M. Schütz, K. Holland and H. Murguia, "Flight Dynamics of Boomerangs: Impact of Drag Force and Drag Torque", AIAA Aviation Forum and Exposition, 2020.

Biography

Ethan Foss graduated from Westview High School in 2019 and is now an undergraduate at the University of California, San Diego, studying Mechanical Engineering with a specialization in Controls and Robotics. He is interested in the Control of Dynamical Systems, particularly optimal trajectory generation and control with application to aerospace vehicles.

Jaime Alvarez received his Bachelor of Science at University of California, San Diego in Electrical Engineering with a focus in Electronic Circuits from 2019 to 2022. During his time here, he led programs and mentored students studying Electrical Engineering to guide and inform them on what the major entails. Currently, he is working as an ATE Test Engineer at Qualcomm and continues to contribute to the growing world of technology.

Todd Hunt graduated from the University of California, San Diego, with a B.S in Aerospace Engineering in 2022. He is currently pursuing an M.S in Aeronautics and Astronautics from Stanford University. His interests include aerodynamics, stability, and structural analysis, related to the testing and verification of aerospace vehicles.

Prasad S. Gudem received the B. Tech degree in Electrical Engineering from the Indian Institute of Technology, Madras, India, in 1988, and the Ph.D. degree in Electrical Engineering from the University of Waterloo, Waterloo, Ontario, Canada, in 1996. He was a Vice President of Engineering at Qualcomm from 2014-2018 and currently an Adjunct faculty in the Department of Electrical and Computer Engineering, University of California at San Diego, La Jolla, CA, USA. He has 50+ patents and 50+ IEEE publications. He taught several graduate-level classes and co-advised twelve Ph.D. students in RF integrated circuit (IC) design. Dr. Gudem was the recipient of the Graduate Teaching Award in recognition of his outstanding teaching of the ECE265 course sequence, “Communication Circuit Design: I, II, and III”. He is an avid follower of the history of STEM (Science, Technology, Engineering, and Mathematics).